ONLINE MATERIAL

APPENDIX A: ASYMMETRIES DIAGNOSTICS FOR SIMULATED DATA

Here we present the asymmetry diagnostics, and the same tests as in Sec. 3.1, for other models.

Time evolution around the buckling event

The buckling instability produces a peak in the time evolution of the buckling amplitude $A_{\rm buck}$ (Debattista et al. 2020; Anderson et al. 2022) and consequently the occurrence of the B/P bulge, which marks the time of the buckling event. In Fig. A1 we present the mid-plane asymmetry profiles traced at high time resolution around the buckling. In particular, we analyse, every 0.1 Gyr, the interval between 3.5 Gyr and 4.5 Gyr. A clear and strong bending of the bar is already visible at 3.5 Gyr, while mid-plane asymmetry starts to be visible at 3.6 Gyr, associated with the typical double-peaked shape of the mid-plane asymmetry profile. Mid-plane asymmetry strongly increases between 3.8-4.0 Gyr, reaching a maximum value of $\mathcal{A}_{\Sigma}(x) \sim 0.45$ at 3.8 Gyr. During this phase, the central portion of the mid-plane asymmetry map, where the B/P bulge appears, is asymmetric as well as producing the four-peaked shape observed in the mid-plane asymmetry profile. At 4 Gyr the B/P bulge is clearly distinguishable from the unsharp mask. After that, the mid-plane asymmetry profiles again show two peaks and they start to slowly decline.

Effect of rotation

In Fig. A2 we present the effect of the rotation procedure ROT on the mid-plane asymmetry diagnostics. The procedure, written in IDL, uses an interpolation method based on a cubic convolution (Park & Schowengerdt 1983).

Effect of the spatial sampling

In Fig. A3 we show the effect of varying the spatial sampling on the mid-plane asymmetry diagnostics.

Effect of the seeing

In Fig. A4 we show the effect of the seeing on the mid-plane asymmetry diagnostics.

Effect of dust

In Fig. A5 we show the face-on, side-on and end-on views of the projected logarithmically-scaled surface number density of the particles of the two models, centred on the origin of the (x, y) plane, with the bar aligned with the x axis, and superimposing some of the isocontours of the dust lanes. We assume for both the dust disc and the dust lanes a double-exponential profile described by Eq. 5. To describe the geometry dust lanes we assume for model D5 $w_{\rm dl}$ = 1.7 kpc, $s_{\rm dl}$ = 15°, $x_{\rm dl,min}$ = −0.3 kpc, and $x_{\rm dl,max}$ = 5.0 kpc, while for model HG1 $w_{\rm dl}$ = 1.2 kpc, $s_{\rm dl}$ = 25°, $x_{\rm dl,min}$ = −0.3 kpc, and $x_{\rm dl,max}$ = 3.0 kpc.

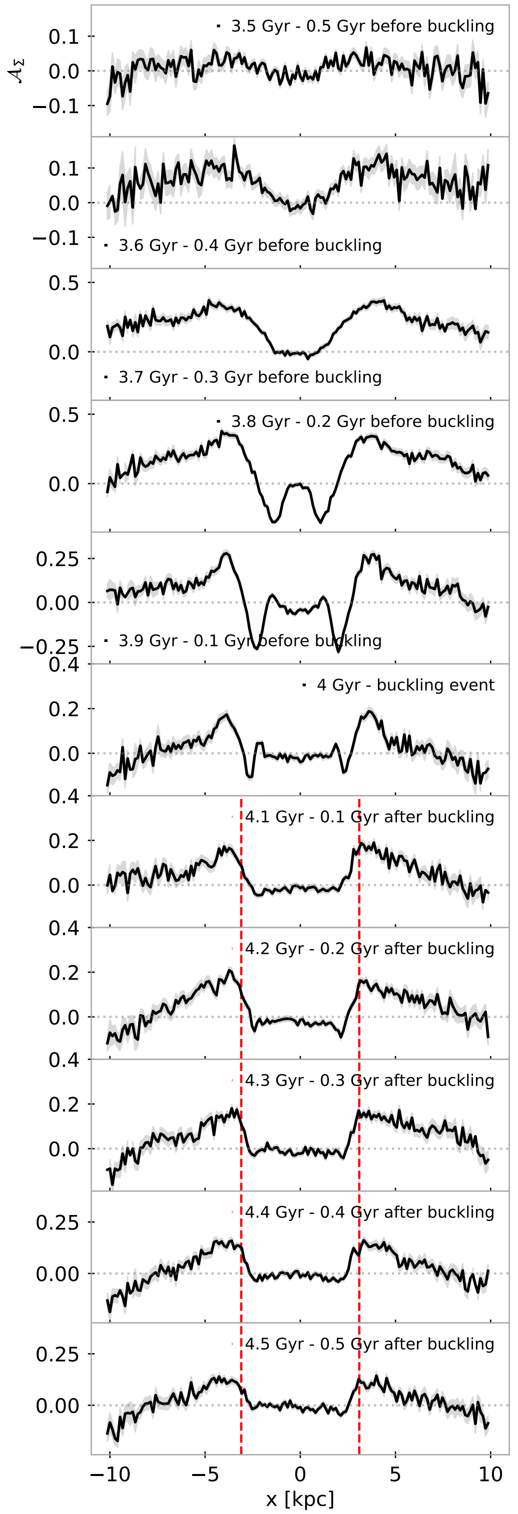

Figure A1. Time evolution of the mid-plane asymmetry radial profile of models D5 over 1 Gyr bracketing the formation of the B/P bulge.

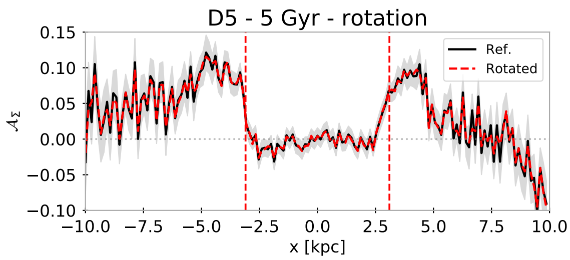

Figure A2. Mid-plane asymmetry profiles as in Fig. 3 lower panel, but for testing the effect of rotation on model D5. The mid-plane asymmetry radial profiles extracted from the original unrotated image of model D5 (at 5 Gyr) seen side-on (black solid line) is compared to that obtained from the rotated image to align the disc position angle to the x axis (red dashed line).

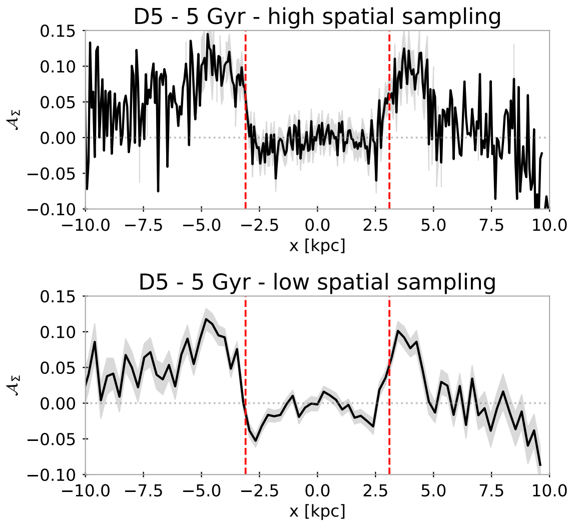

Figure A3. Mid-plane asymmetry profiles as in Fig. 3 lower panel, but for model D5 (at 5 Gyr) mapped with a 2× better spatial sampling (0.065 kpc pixel^{-1}, upper panel) and with a 2× worse spatial sampling (0.26 kpc pixel^{-1}, lower panel).

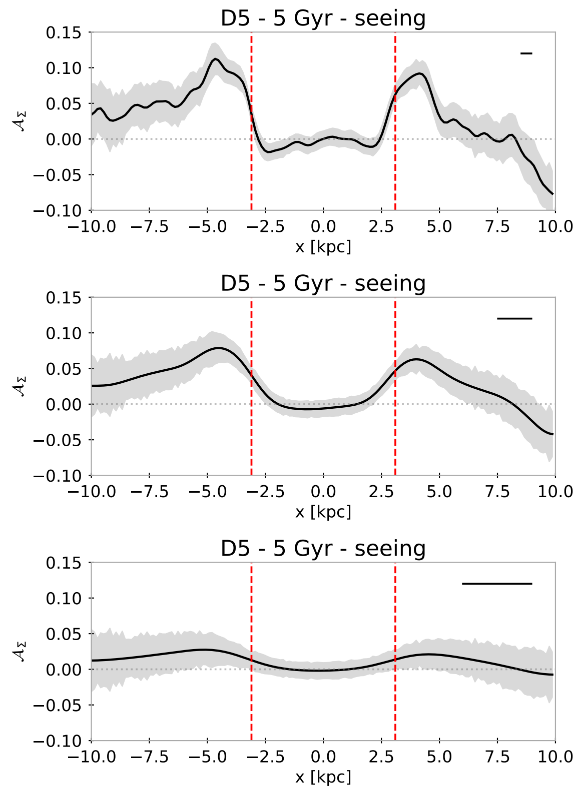

Figure A4. Same as Fig. 3 lower panel, but for model D5 (at 5 Gyr) after convolving the image of the projected number density of the particles rescaled at a distance of 50 Mpc with a Gaussian filter with a FWHM=0.5 kpc (corresponding to 2.1 arcsec, upper panel), 1.5 kpc (6.3 arcsec, central panel), and 3.1 kpc (12.6 arcsec, lower panel). The horizontal black segments at top right in each panel indicate the adopted FWHM.

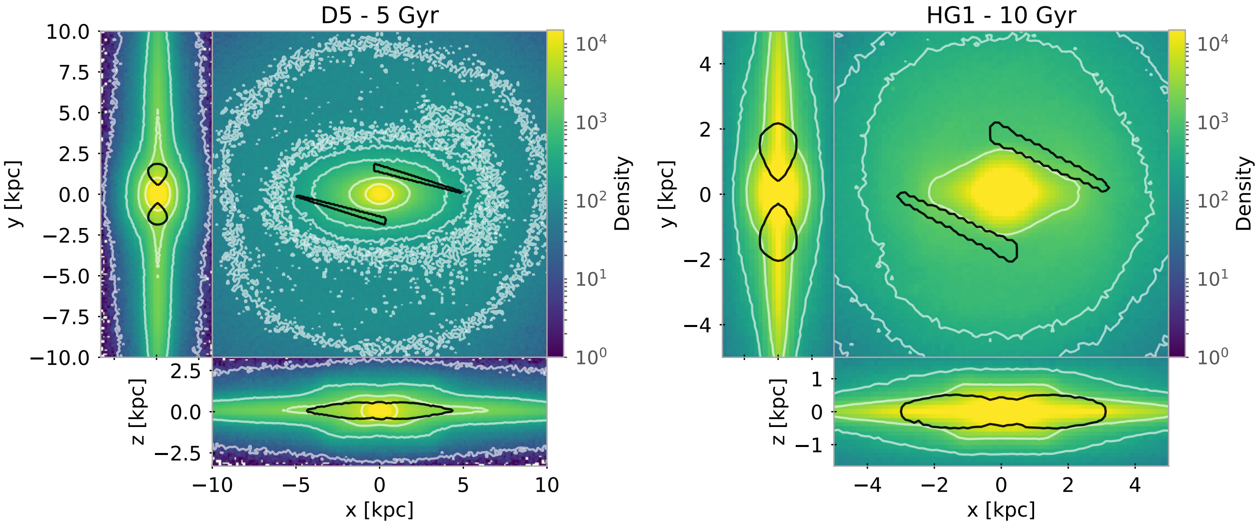

Figure A5. Same as Fig. 1 but with some isocontours of the surface number density (black lines) of the dust lanes for each viewing geometry.

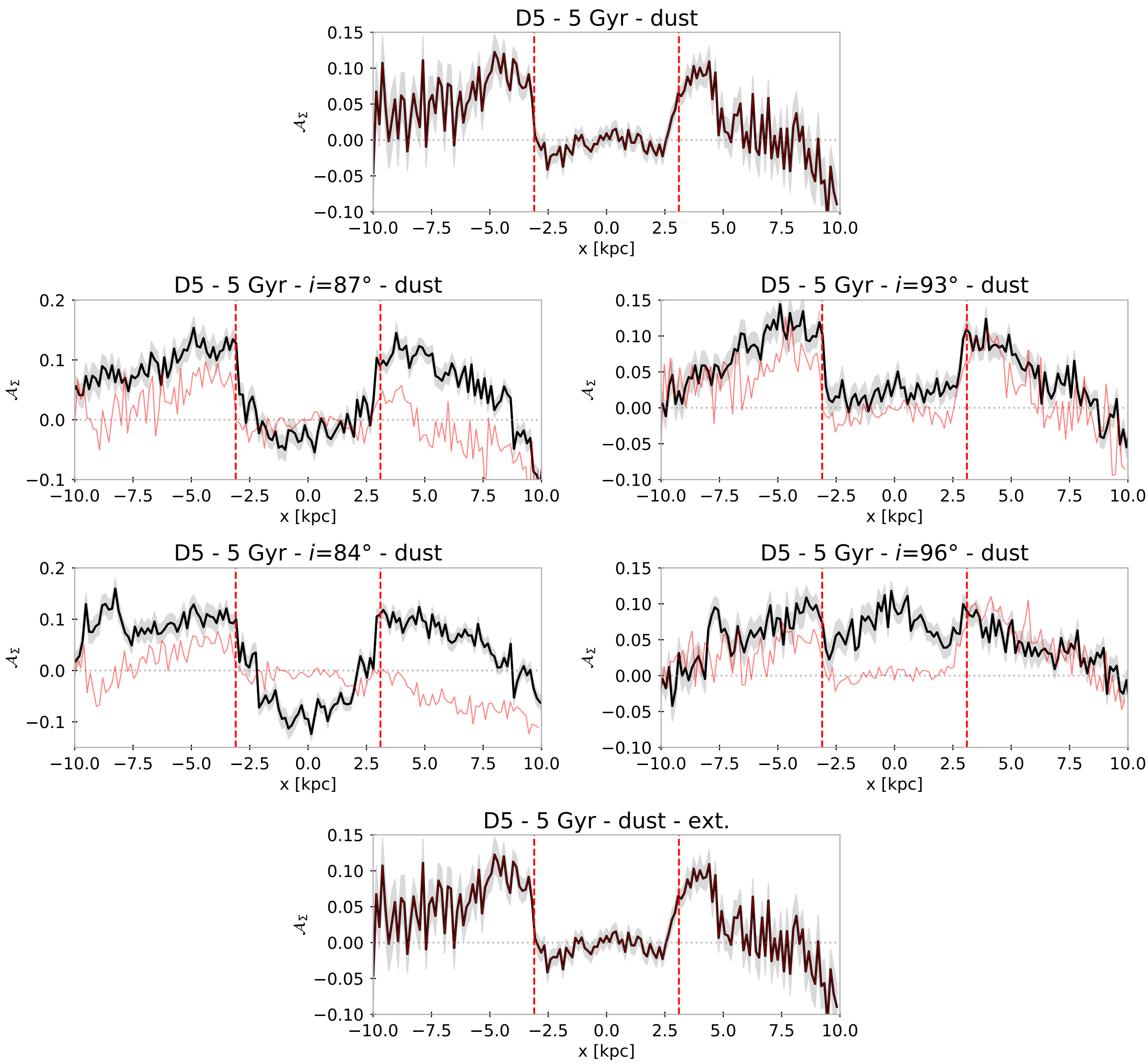

Figure A6. Mid-plane asymmetry profiles as in Fig. 3 lower panel, but for model the D5 (at 5 Gyr) after taking into account the effect of the dust (disc with $h_{\rm R,disc}$ = 1 kpc and $h_{\rm z,disc}$ = 0.1 kpc + dust lanes), with different inclinations with respect to the side-on view (i = 90°, first row; $\Delta i \pm 3°$, second row row; $\Delta i \pm 6°$, third row) and with a radially very extended dust disc with $h_{\rm R,disc}$ = 1.5× initial galaxy disc scalelength (i = 90°, fourth row). Superimposed in red are shown the corresponding profiles obtained without taking into account the effect of the dust.

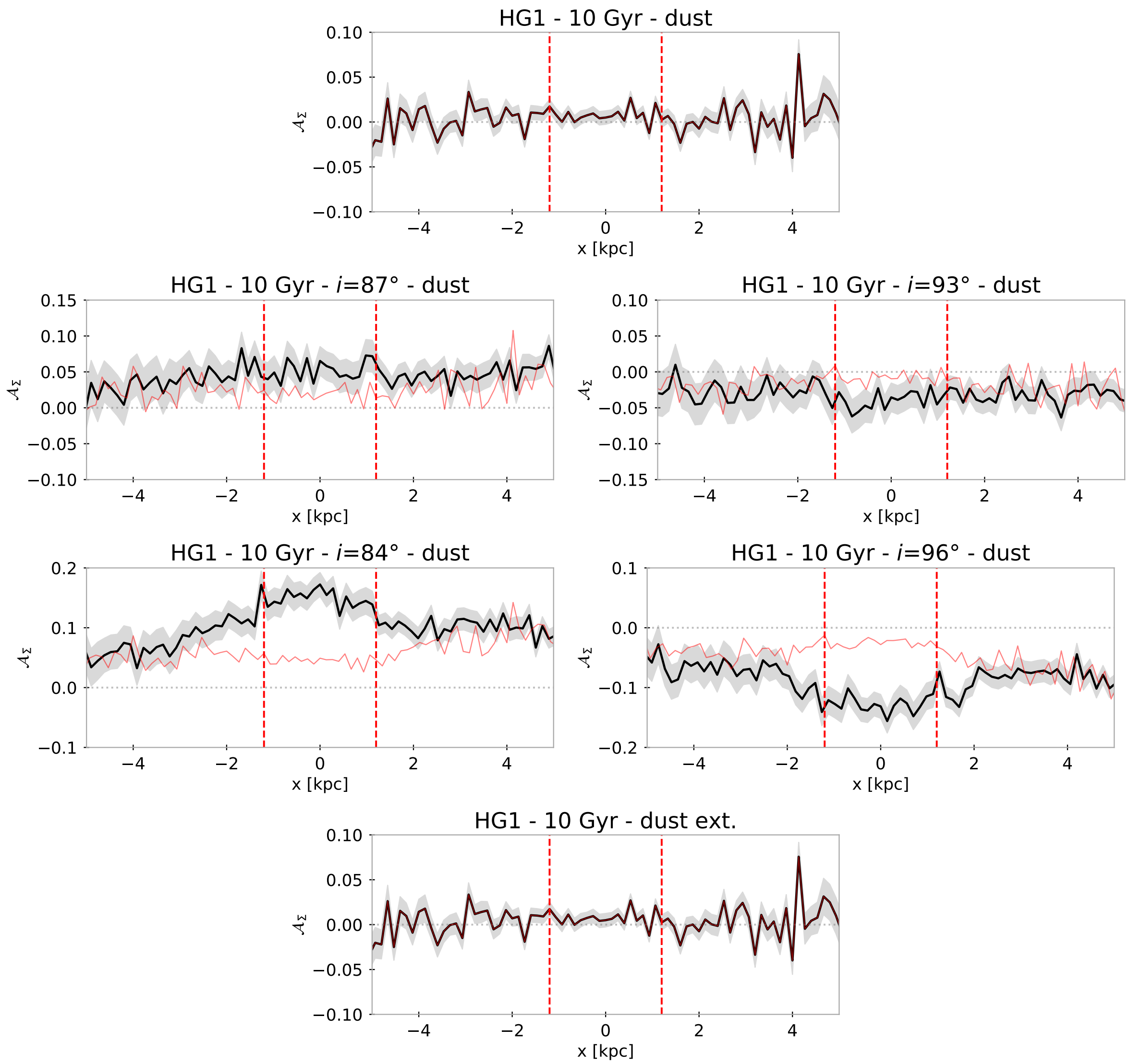

Figure A7. Mid-plane asymmetry profiles as in Fig. 3 lower panel, but for model the HG1 (at 10 Gyr) after taking into account the effect of the dust (disc with $h_{\mathrm{R,disc}}$ = 1 kpc and $h_{\mathrm{z,disc}}$ = 0.1 kpc + dust lanes), with different inclinations with respect to the side-on view (i = 90°, first row; $\Delta i \pm 3°$, second row row; $\Delta i \pm 6°$, third row) and with a radially very extended dust disc with $h_{\mathrm{R,disc}}$ = 1.5× initial galaxy disc scalelength (i = 90°, fourth row). Superimposed in red are shown the corresponding profiles obtained without taking into account the effect of the dust.

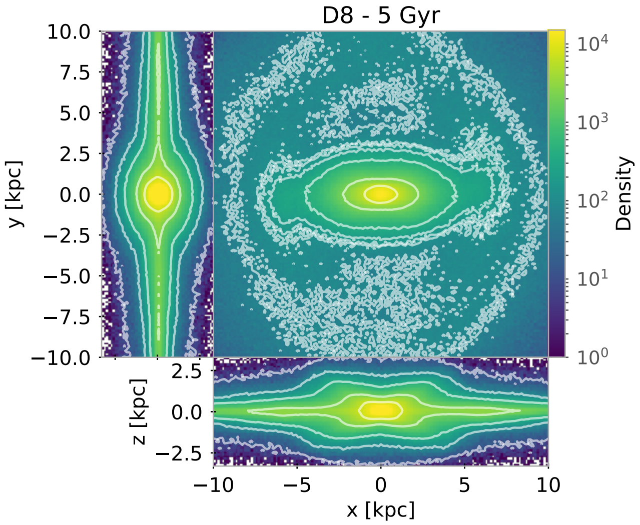

Figure A8. Same as Fig. 1, but for model D8.

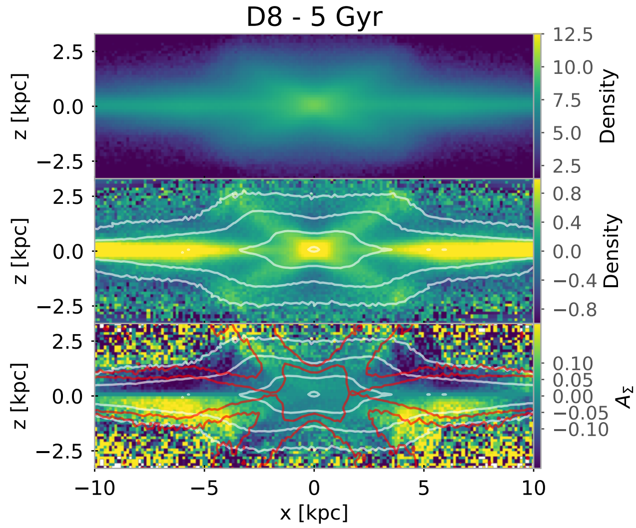

Figure A9. Same as Fig. 2, but for model D8.

Model D8

Model D8 is a pure N-body one, presented in Anderson et al. (2022). It suffered from a first and weak buckling event at 1.5 Gyr ($A_{\rm buck}$ ~ 0.015 kpc), after which it develops a B/P bulge, and a second buckling event at 4 Gyr ($A_{\rm buck}$ ~ 0.04 kpc), after which it develops strong asymmetries. After the second buckling event the bar grows constantly (from $A_{\rm bar}$ ~ 0.2 to ~ 0.3) till the end of the simulation (10 Gyr). In the following plots we describe the asymmetries visible at 5 Gyr (1 Gyr after the second buckling event). The B/P bulge has a semi-major axis of 3.5 kpc and a semi-minor one of 2.5 kpc.

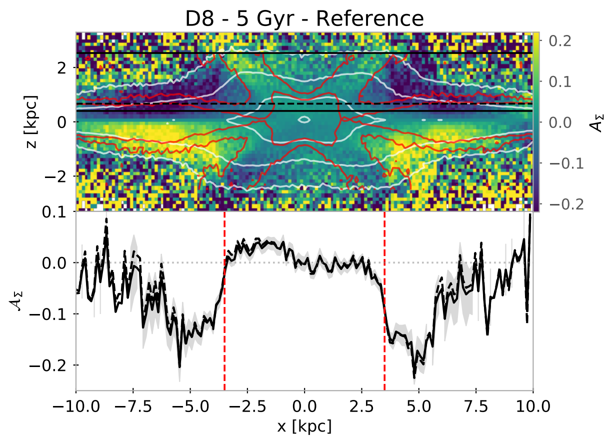

Figure A10. Same as Fig. 3, but for model D8 (at 5 Gyr) with $0.4 < z < 2.5$ kpc (solid line) and $0.7 < z < 2.5$ kpc (dashed line).

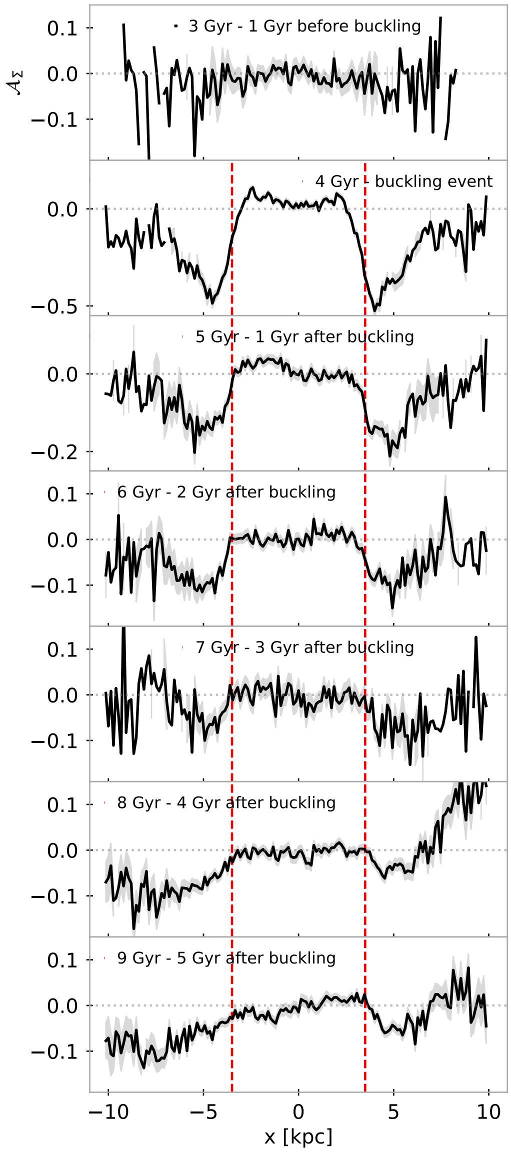

Figure A11. Same as Fig. 4 but for model D8.

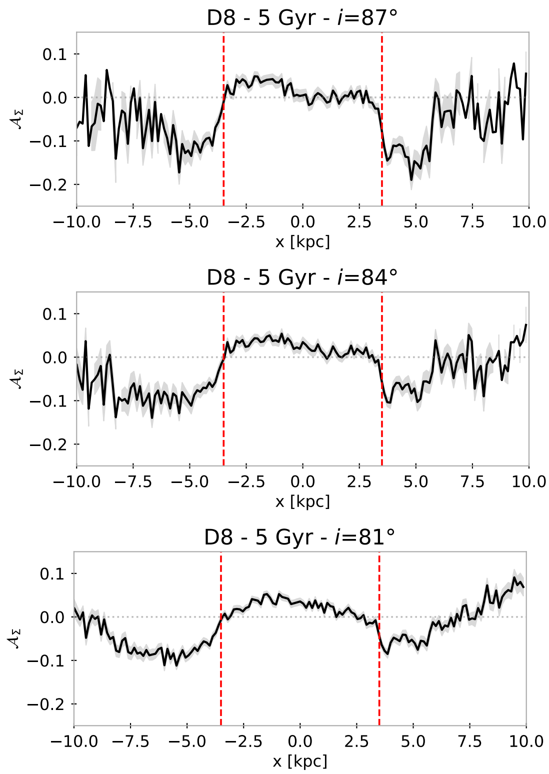

Figure A12. Same as Fig 5, but for model D8.

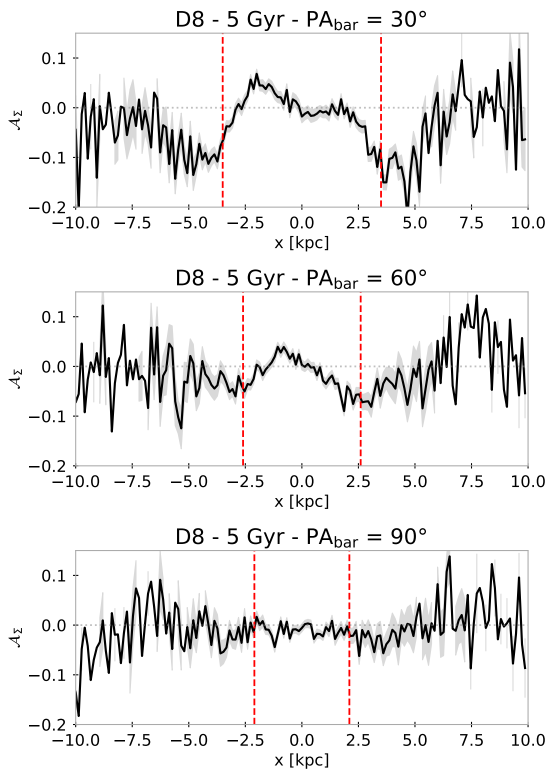

Figure A13. Same as Fig 7, but for model D8.

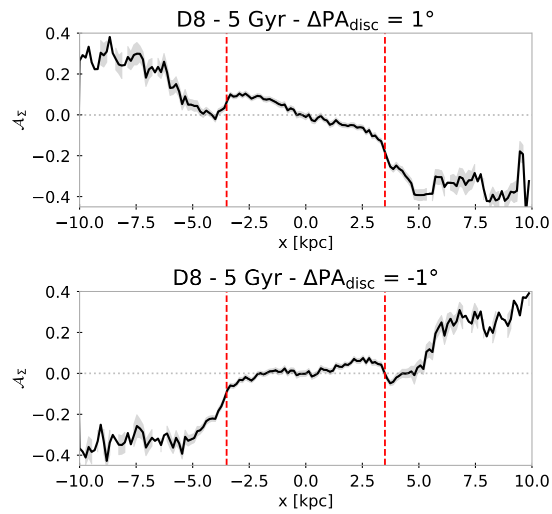

Figure A14. Same as Fig 8, but for model D8.

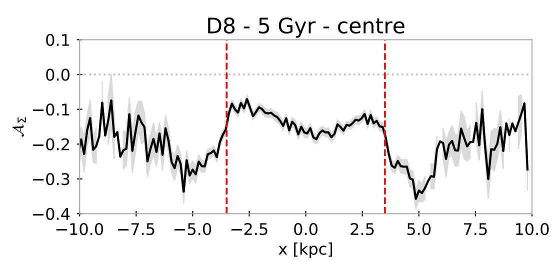

Figure A15. Same as Fig 10, but for model D8.

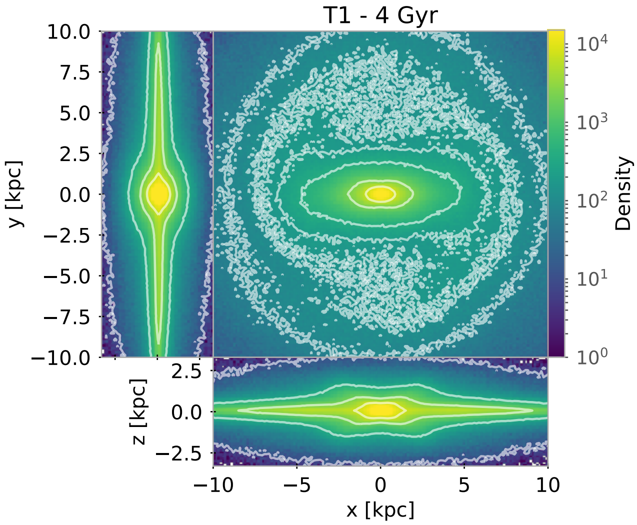

Figure A16. Same as Fig. 1, but for model T1 at 4 Gyr, i.e. 1.5 Gyr after the mild buckling event.

Model T1

Model T1 is a pure N-body one, presented in Anderson et al. (2022). It suffered from a mild buckling event at 1.5 Gyr ($A_{\rm buck} \sim 0.02$), after which it develops a B/P bulge while the bar grows constantly (from $A_{\rm bar} \sim 0.1$ to ~ 0.25) till the end of the simulation (10 Gyr). The model develops strong asymmetries just after the buckling event (at 2 Gyr) but they quickly disappear (they are no longer visible at 5 Gyr). In the following plots we describe the asymmetries visible at 2 Gyr and in comparison the corresponding plots at 4 Gyr. The B/P bulge has a semi-major axis of 2.5 kpc and a semi-minor one of 2.1 kpc.

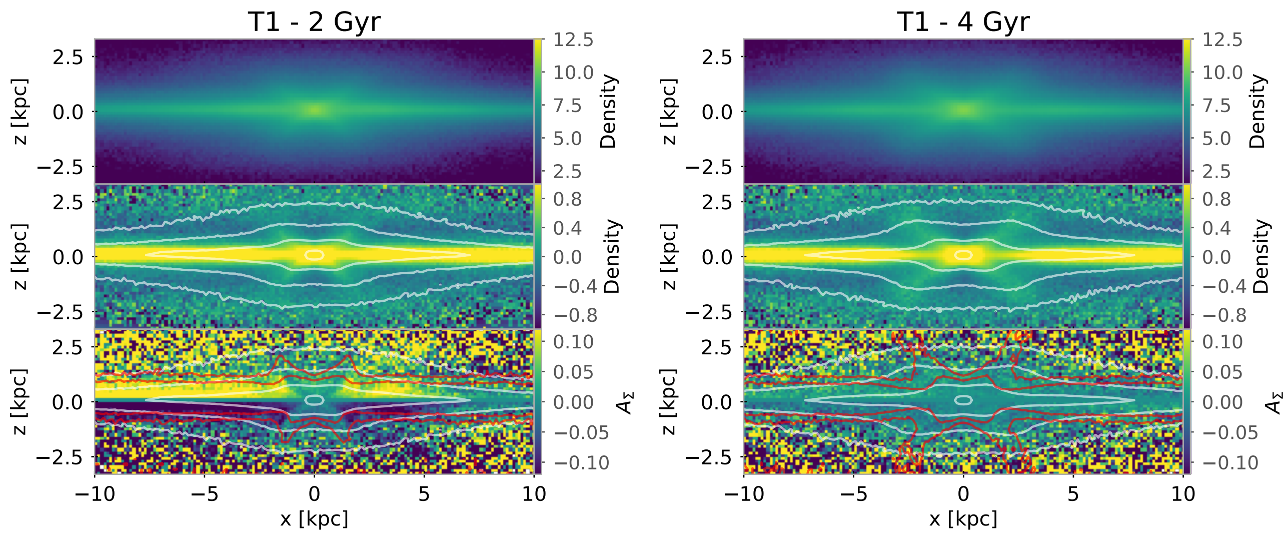

Figure A17. Same as Fig. 2, but for model T1 at 2 Gyr (left-hand column) and 4 Gyr (right-hand column).

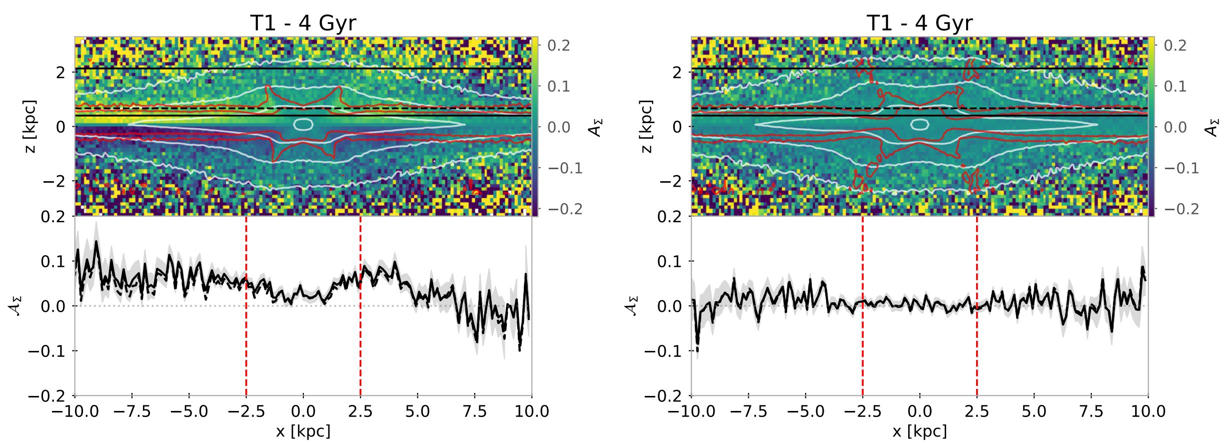

Figure A18. Same as Fig. 3, but for model T1 at 2 Gyr (left-hand column) and 4 Gyr (right-hand column) with $0.3 < z < 2.1$ kpc.

Model SD1

Model SD1 is a pure N-body one, presented in Anderson et al. 2022. It develops a B/P bulge without suffering a strong buckling event ($A_{\rm buck}$ remains below 0.008 kpc). The bar grows constantly reaching $A_{\rm bar} \sim 0.25$ at the end of the simulation (10 Gyr). No asymmetries are visible during the formation and evolution of the B/P bulge. Here we present the results at 6 Gyr: the disc hosts asymmetric spiral arms, while the outermost region of the disc is warped: this explains the asymmetry appearing at the end of the evolution. The B/P bulge has a semi-major axis of 3.3 kpc and a semi-minor one of 2.6 kpc.

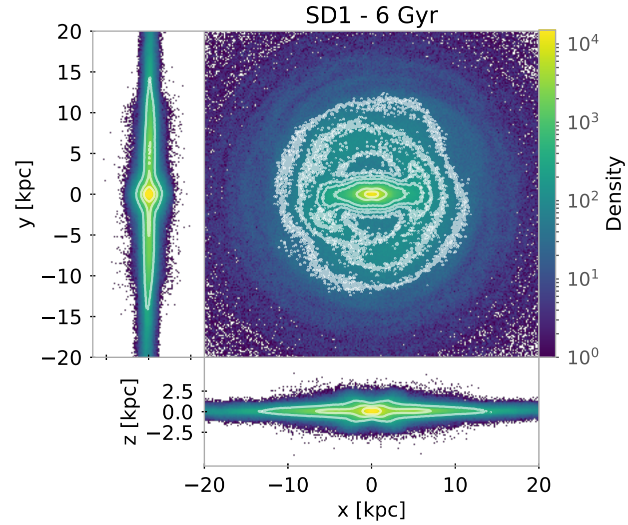

Figure A19. Same as Fig. 1, but for model SD1.

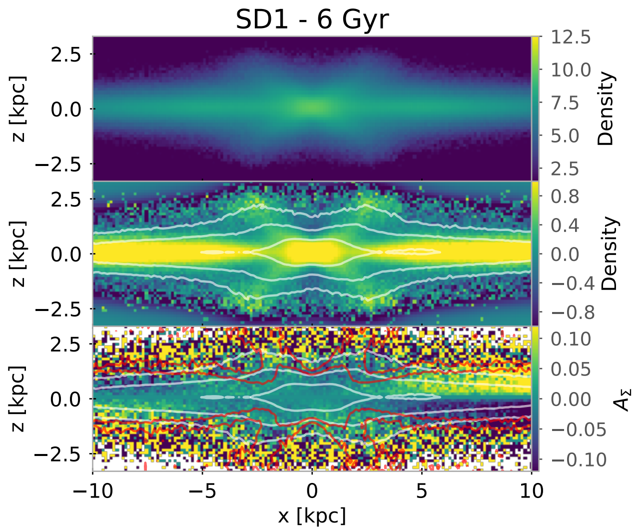

Figure A20. Same as Fig. 2, but for model SD1.

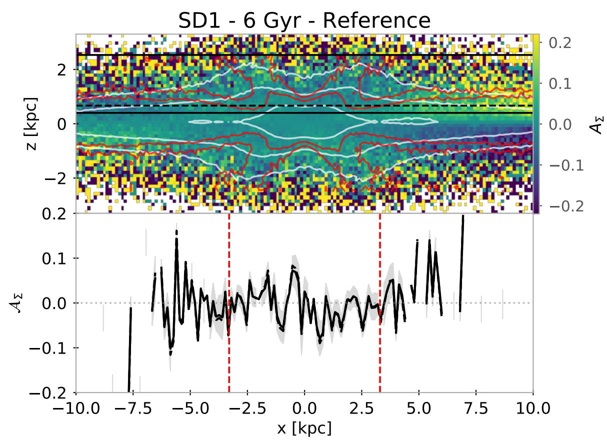

Figure A21. Same as Fig. 3, but for model SD1 (at 6 Gyr) with $0.7 < z < 2.6$ kpc (solid line) and $0.4 < z < 2.6$ kpc (dashed line).

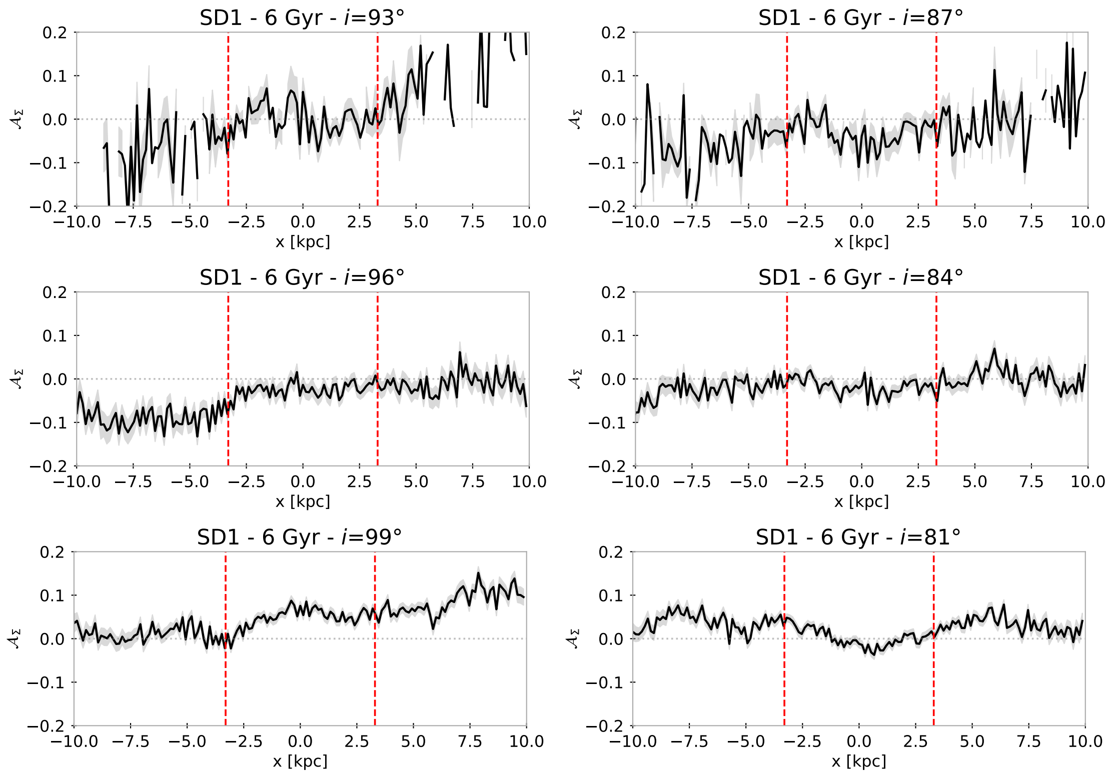

Figure A22. Same as Fig 5, but for model SD1.

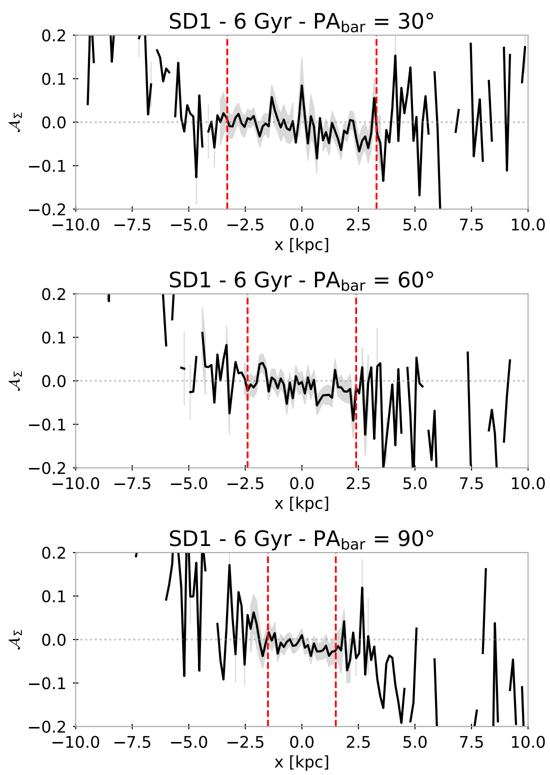

Figure A23. Same as Fig 7, but for model SD1.

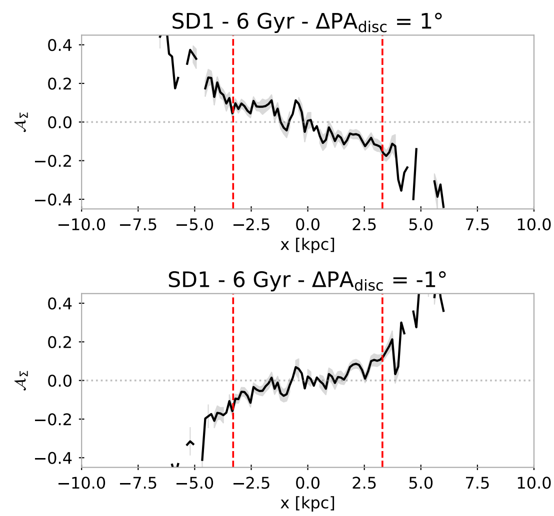

Figure A24. Same as Fig 8, but for model SD1.

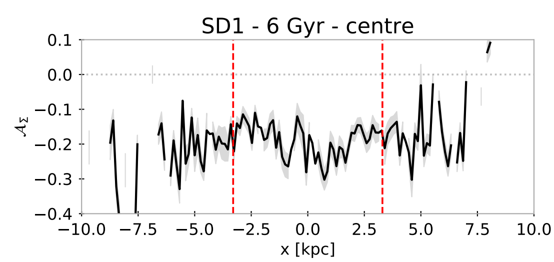

Figure A25. Same as Fig 10, but for model SD1.

APPENDIX B: MID-PLANE ASYMMETRY DIAGNOSTICS FOR THE DISCARDED GALAXIES

Four of the eight edge-on galaxies we selected from the S^{4}G catalog were discarded from the parent sample because of difficulties in analysing them. Here we present the mid-plane asymmetry diagnostics for these four galaxies. Table 1 gives the reason why each of these galaxies was discarded.

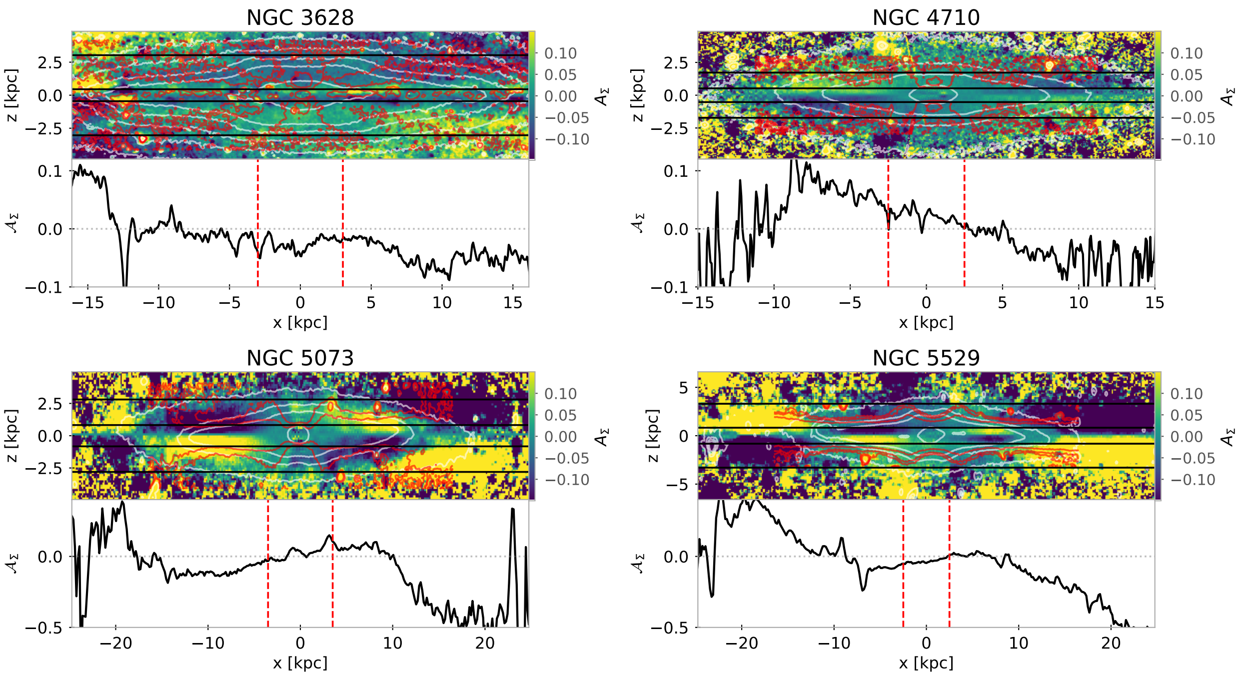

Figure B1. Same as Fig. 14, but for the galaxies excluded from the final sample. Top-left panel: NGC 3628 with $0.5 < z < 3.0$ kpc. Top-right panel: NGC 4710 with $0.5 < z < 2.7$ kpc. Bottom-left panel: NGC 5073 with $0.8 < z < 2.8$ kpc. Bottom-right panel: NGC 5529 with $0.8 < z < 3.3$ kpc.

APPENDIX C: MID-PLANE ASYMMETRY DIAGNOSTICS FOR THE STELLAR MASS MAPS OF THE GALAXIES

Mid-plane asymmetry diagnostics for two of our final sample of galaxies obtained using the stellar mass maps of the galaxies. No stellar image is available for NGC 5170, while the image of ESO 443-042 is not suitable for this analysis.

This paper has been typeset from a TEX/LATEX file prepared by the author.

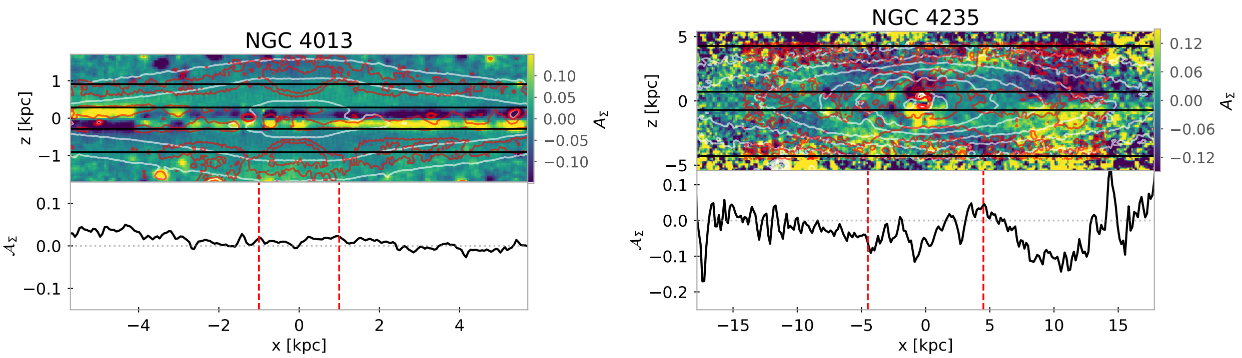

Figure C1. Same as Fig. 14, but using the stellar mass map. Left panel: NGC 4013 with $0.3 < z < 1.0$ kpc. Right panel: NGC 4235 with $0.7 < z < 4.2$ kpc.